

# A DETERMINATION OF DARK MATTER BISPECTRUM WITH A LARGE SET OF $N$ -BODY SIMULATIONS

H. GUO<sup>1,2</sup>, Y. P. JING<sup>1</sup>

*Draft version September 7, 2018*

## ABSTRACT

We use a set of numerical  $N$ -body simulations to study the large-scale behavior of the reduced bispectrum of dark matter and compare the results with the second-order perturbation theory and the halo models for different halo mass functions. We find that the second-order perturbation theory (PT2) agrees with the simulations fairly well on large scales of  $k < 0.05 h\text{Mpc}^{-1}$ , but it shows a signature of deviation as the scale goes down. Even on the largest scale where the bispectrum can be measured reasonably well in our simulations, the inconsistency between PT2 and the simulations appears for the colinear triangle shapes. For the halo model, we find that it can only serve as a qualitative method to help study the behavior of  $Q$  on large scales and also on relatively small scales. The failure of second-order perturbation theory will also affect the precise determination of the halo models, since they are connected through the 3-halo term in the halo model. The 2-halo term has too much contribution on the large scales, which is the main reason for the halo model to overpredict the bispectrum on the large scales. Since neither of the models can provide a satisfying description for the bispectrum on scales  $k \sim 0.1 h\text{Mpc}^{-1}$  for the requirement of precision cosmology, we release the reduced bispectrum of dark matter on a large range of scales for future analytical modeling of the bispectrum.

*Subject headings:* gravitational lensing—dark matter— cosmology: theory— galaxies: formation

## 1. INTRODUCTION

The understanding of the formation, clustering, and evolution of galaxies needs to involve the dark matter in modern cosmological models. In the current standard paradigm, i.e.,  $\Lambda$  cold dark matter (CDM) models, dark matter has negligible velocity in the early universe and dominates the matter density in the present universe. Starting from an initially tiny Gaussian density fluctuation, the density distribution of CDM would keep its Gaussianity throughout the whole evolution in the linear-order perturbation (e.g., Peebles 1980; Bernardeau et al. 2002; Sefusatti & Komatsu 2007). However, the dynamical evolution of the fluctuations, through the mode coupling of different scales, would result in non-Gaussianity of density distribution on all scales, including the conventional linear regime. Various statistical tools are used in the literature to describe the density distribution, and can be further incorporated into the research of non-Gaussianity. For example, the two-point correlation function (2PCF)  $\xi(r)$  is employed to describe the correlation of two objects at a separation  $r$ , while the three-point correlation function (3PCF) is used to describe the next-order statistics in the series of connected  $N$ -point correlation functions (NPCFs) (Peebles 1980). In the linear-order perturbation theory, a Gaussian field is completely determined by the 2PCF. Therefore, the 3PCF is the lowest-order non-Gaussian quantity in the series, which can give us important clues to the properties of nonlinear evolution.

The dark matter 3PCF and its Fourier-space counter-

part, the bispectrum, have been studied intensively over the years (e.g., Fry 1984; Scoccimarro et al. 1998; Hou et al. 2005; Nichol et al. 2006). The theoretical work mainly comprises two methods: the nonlinear perturbation theory (hereafter PT; e.g., Bernardeau et al. 2002, and the references therein) and the halo model (hereafter HM; Jing & Börner 1998; Ma & Fry 2000; Peacock & Smith 2000; Seljak 2000; Scoccimarro et al. 2001; Takada & Jain 2003; Yang, Mo, & van den Bosch 2003; Wang et al. 2004; Smith et al. 2008). Both methods have been applied to and compared with simulations over a range of scales (e.g., Scoccimarro et al. 2001; Hou et al. 2005; Smith et al. 2008). In addition, as a prior assumption, PT is believed to be applicable on large scales where the density fluctuation is small enough for a perturbative method to be useful. It starts to fail as the scale goes down to the strongly nonlinear regime.

The halo model approach, however, is based upon dark matter halos. By utilizing halo correlation functions and the dark matter distribution in the halos, the halo model can then generate the dark matter clustering statistics without any consideration of the scales. An advantage of the halo model method is that after being combined with the models of galaxy distribution in the host halos, which is often called halo occupation distribution (HOD; e.g., Jing et al. 1998; Berlind & Weinberg 2002; Yang, Mo, & van den Bosch 2003; Zehavi et al. 2004; Zheng 2004; Zheng et al. 2005), it can produce the overall distribution of galaxies, which can be directly compared with the observations of large-scale galaxy surveys. So, the halo model method can also be used to predict the galaxy-biasing relations (e.g., Seljak 2000; Scoccimarro et al. 2001; Verde et al. 2002).

The development of numerical simulations in recent years helps test the validity and range of applicability of these theories (e.g., Scoccimarro et al. 2001; Fosalba et

<sup>1</sup> Key Laboratory for Research in Galaxies and Cosmology, Shanghai Astronomical Observatory, Chinese Academy of Sciences, Nandan Road 80, Shanghai 200030, China; guoh@shao.ac.cn, ypjing@shao.ac.cn.

<sup>2</sup> Graduate School of the Chinese Academy of Sciences, 19A, Yuquan Road, Beijing, China

al. 2005; Smith et al. 2008). On large scales, both PT and HM are believed to be in good agreement with the simulations. On smaller scales (quasi-linear and nonlinear regimes), PT breaks down fairly quickly, while HM may still be a good approximation. However, most of the previous simulation studies in the literature only measure the bispectrum on the scales smaller than that of  $k \sim 0.1 h\text{Mpc}^{-1}$ , due to the limited dynamical range of their simulations.

In this work, we use a set of high-resolution large-box cosmological  $N$ -body simulations to accurately determine the dark matter bispectrum on both large and small scales. The results will be compared with the predictions of PT and HM in order to test their validity in describing the bispectrum. It is important to determine where and how well the theories are valid, since a determination of the galaxy bispectrum in observation can yield a determination of the galaxy bias factors on large scales if the bispectrum of dark matter can be predicted (e.g., Fry 1984; Fry et al. 1993). As we will see that neither the second-order PT (hereafter PT2; without loop corrections) nor the HM can provide a satisfying description for the dark matter bispectrum on scales of  $k \sim 0.1 h\text{Mpc}^{-1}$  in the standard of precision cosmology, we make the bispectrum of dark matter on a large range of scales available to interested readers, who want to use the data to construct a more accurate model for the bispectrum.

This paper is organized as follows. In Section 2, we describe some basic formulae and the method used in this paper. We introduce our simulations in Section 3. We compare the simulations with PT and halo models in Section 4.1 and Section 4.2, respectively. We summarize our results in Section 5.

## 2. METHODS

In a statistically homogeneous and isotropic universe, the density fluctuation of the matter distribution is defined as  $\delta(\mathbf{x}) = (\rho(\mathbf{x}) - \bar{\rho})/\bar{\rho}$ , with the mean density being  $\bar{\rho} = \langle \rho(\mathbf{x}) \rangle$ . Due to the convenience in calculating bispectrum in Fourier space, we transform  $\delta(\mathbf{x})$  to

$$\delta_{\mathbf{k}} = \int d^3x \exp(-i\mathbf{k} \cdot \mathbf{x}) \delta(\mathbf{x}). \quad (1)$$

By definition  $\langle \delta_{\mathbf{k}} \rangle = 0$ . So the next two nonvanishing terms in the series will be

$$\langle \delta_{\mathbf{k}_1} \delta_{\mathbf{k}_2} \rangle = \delta^D(\mathbf{k}_1 + \mathbf{k}_2) P(k_1) \quad (2)$$

$$\langle \delta_{\mathbf{k}_1} \delta_{\mathbf{k}_2} \delta_{\mathbf{k}_3} \rangle = \delta^D(\mathbf{k}_1 + \mathbf{k}_2 + \mathbf{k}_3) B(k_1, k_2, k_3), \quad (3)$$

where  $\delta^D(\mathbf{k})$  is the three-dimensional Dirac delta function and  $P(k)$  and  $B(k_1, k_2, k_3)$  are the Fourier transform of the 2PCF and 3PCF, known as the power spectrum and bispectrum, respectively. If we extend the perturbation theory to the second order, it gives (Fry 1984; Bernardeau et al. 2002)

$$B_{PT}(k_1, k_2, k_3) = F(\mathbf{k}_1, \mathbf{k}_2) P_L(k_1) P_L(k_2) + cyc, \quad (4)$$

$$F(\mathbf{k}_1, \mathbf{k}_2) = (1 + \mu) + \frac{\mathbf{k}_1 \cdot \mathbf{k}_2}{k_1 k_2} \left( \frac{k_1}{k_2} + \frac{k_2}{k_1} \right)$$

$$+ (1 - \mu) \left( \frac{\mathbf{k}_1 \cdot \mathbf{k}_2}{k_1 k_2} \right)^2, \quad (5)$$

where  $P_L(k)$  is the linear power spectrum and  $\mu = 3\Omega_m^{-2/63}/7$  denotes the weak dependence on cosmology.

It is often convenient to define the reduced bispectrum,

$$Q(k_1, k_2, k_3) = \frac{B_{PT}(k_1, k_2, k_3)}{P_L(k_1) P_L(k_2) + cyc}, \quad (6)$$

where  $k_1$ ,  $k_2$ , and  $k_3$  set the three sides of the triangle shape. Two sets of variables are frequently used for  $Q$ . We define the three variables to be  $k = k_1$ ,  $u = k_2/k_1$ , and  $v = (k_3 - k_2)/k_1$ , where  $k_1 \leq k_2 \leq k_3$ ,  $u \geq 1$ , and  $0 \leq v < 1$ . Therefore,  $k$  sets the scale of the triangle, while  $u$  and  $v$  determine its shape. In addition, if we change  $v$  to  $\alpha = \arccos(\mathbf{k}_1 \cdot \mathbf{k}_2)/k_1 k_2$ , ( $0 < \alpha < \pi$ ), we get the other form as  $Q(k, u, \alpha)$ , which clearly shows the relation between  $k_1$  and  $k_2$ . Also, the shape dependence is obviously described by  $u$  and  $\alpha$ . But this parametrization has a disadvantage that when considering triangles of different scales and different shapes together, we may have counted the set of  $(k_1, k_2, k_3)$  repeatedly, because in this case we only have  $0 < k_3 < k_1 + k_2$ . In order to avoid repeated counting, we still need to impose a constraint of  $k_3 \geq k_2$  when we count independent triangles. We will use  $Q(k, u, \alpha)$  as the preferred parametrization when investigating the scale and shape dependence of  $Q$  in the following sections.

Although  $Q(k, u, \alpha)$  is generally dependent on the scale and shape of a triangle, in the second-order perturbation theory, if we assume the power spectrum to be a power law,  $Q$  is then completely independent on the scale  $k$ . For the equilateral triangle shapes  $k_1 = k_2 = k_3$ , from Equations (4) and (6) we have  $Q_{eq} = 1/4 + 3\mu/4$ , which is exactly constant. These important properties of the reduced bispectrum  $Q$  make it a better quantity than the bispectrum  $B(k_1, k_2, k_3)$  to characterize the non-Gaussianity of the matter distribution. The shape dependence of  $Q$  reflects the influence of the gravitational instability, so it can be significantly affected by the existence of large-scale structures such as filaments (Sefusatti & Scoccimarro 2005) for small simulation volumes. In order to reduce such finite-volume effects, large-box simulations are necessary to compute the bispectrum as we do in this paper.

## 3. N-BODY SIMULATIONS

The cosmological model considered here is a canonical spatially flat CDM model with the density parameter  $\Omega_m = 0.268$ , the cosmological constant  $\Omega_\Lambda = 0.732$ , the Hubble constant  $h = 0.71$ , and the baryon density parameter  $\Omega_b = 0.045$ . The primordial density field is assumed to be Gaussian with a scale-invariant power spectrum  $\propto k$ . For the linear spectrum, we generate it from the CMBfast code (Seljak & Zaldarriaga 1996), and the normalization is set by  $\sigma_8 = 0.85$ , where  $\sigma_8$  is the present linear rms density fluctuation within a sphere of radius  $8 h^{-1} \text{Mpc}$ .

We use an upgraded version of the Particle-Particle-Particle-Mesh ( $P^3M$ ) code of Jing & Suto (1998, 2002) to simulate structure formation in the universe. The code has now incorporated the multiple level  $P^3M$  gravity solver for high-density regions (Jing & Suto 2000).

TABLE 1  
SIMULATION PARAMETERS

boxsize( $h^{-1}\text{Mpc}$ )	particles	realizations	$m_{\text{particle}}$
600	$1024^3$	3	$1.5 \times 10^{10} h^{-1} M_{\odot}$
1200	$1024^3$	4	$1.2 \times 10^{11} h^{-1} M_{\odot}$
1800	$1024^3$	4	$4.0 \times 10^{11} h^{-1} M_{\odot}$

In order to have a large mass resolution range, we run a total of 11 simulations with  $1024^3$  particles in different simulation boxes, which we hereafter denote by  $L600$ ,  $L1200$ , and  $L1800$  by different box sizes (Table 1) (Jing et al. 2007). The simulations were run on an SGI Altix 350 with 16 processors with OPENMP parallelization in Shanghai Astronomical Observatory.

The different box sizes put different limits on the detection scales in the simulations, which is  $k \geq k_{\text{box}} = 2\pi/L_{\text{box}}$ . For our simulations here, we have  $k_{\text{box}} = 0.0035, 0.0052, 0.01 h\text{Mpc}^{-1}$  for  $L1800$ ,  $L1200$ , and  $L600$ , respectively. Thus, in principle, we expect to determine the behavior of the dark matter bispectrum on scales larger than  $k = 0.1 h\text{Mpc}^{-1}$  with good precision. The large resolution range used here enables us to check the consistency of the results among different simulation boxes and to investigate the behavior of dark matter bispectrum down to small scales. Here, we choose the bin scheme as  $\Delta \log_{10}(k) = 0.1$  for  $k < 0.1 h\text{Mpc}^{-1}$  and 0.05 for the larger  $k$  in Fourier space. But even for  $L1800$ , we only have four realizations, which may still be not enough to recover the exact variance of the bispectrum on large scales. So, we calculate the uncertainty of bispectrum under the assumption of a Gaussian field as (e.g., Fry et al. 1993; Scoccimarro et al. 1998, 2004; Sefusatti & Komatsu 2007)

$$\Delta B_{123}^2 = \frac{1}{N_{123}} P_{\text{tot}}(k_1) P_{\text{tot}}(k_2) P_{\text{tot}}(k_3)$$

$$P_{\text{tot}}(k) = P(k) + \frac{1}{N_p}, \quad (7)$$

where  $N_{123}$  is the number of independent triangle configuration modes in the Fourier space, and  $P_{\text{tot}}(k)$  is the power spectrum that includes the contribution of shot noise with  $N_p$  particles. Compared with Equation (28) in Sefusatti & Komatsu (2007), there is no  $s_{123}$  factor in our Equation (7) since  $N_{123}$  is the number of independent triangle modes and the statistically rotational-invariance effect has already been taken into account.

We show the ratios between the variances of the mean of the reduced bispectrum averaged over the realizations and the corresponding uncertainties of a Gaussian field (Equation (7)) in Figure 1, where different panels stand for different simulation boxes. The scale  $k$  shown in Figure 1 is defined to be the longest side of the triangle. In addition, to make a complete statistics of the variance ratio, we have included all the triangle configurations in each  $k$  bin. On large scales of  $k \lesssim 0.2 h\text{Mpc}^{-1}$ , the Gaussian uncertainties are slightly larger than those determined from different simulation realizations, with  $\sigma_{\text{sim}}/\sigma_{\text{gaussian}} \approx 0.9$ . This is probably due to the fact that we have used  $P(k)$  determined from the simulations to normalize the bispectra (see Equation (6)). As the

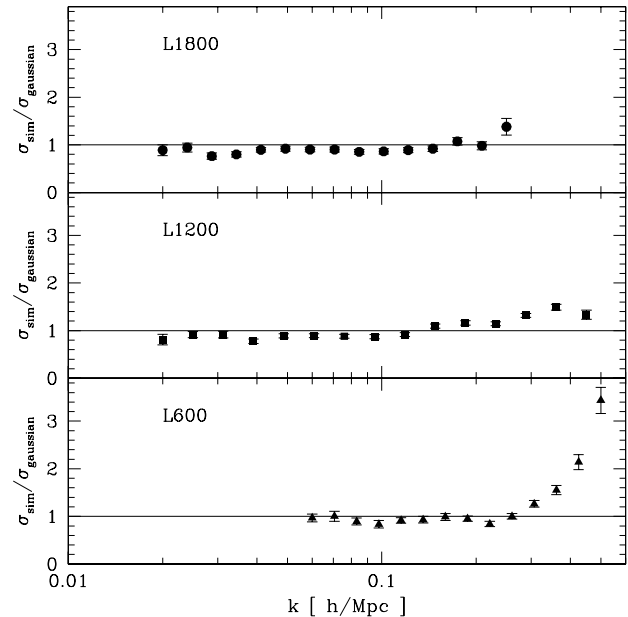


FIG. 1.— Ratios between the variances of the mean of the reduced bispectrum averaged over the realizations and the theoretical Gaussian uncertainties. Different panels stand for different simulation boxes. The scale  $k$  is defined to be the longest side of a triangle.

scale goes down to the nonlinear scales where the assumption of a Gaussian field is not applicable, the ratio increases rapidly, as shown in the case of  $L600$ . So, for our purposes here, the utilization of Gaussian variance on the large scales can, to some extent, compensate for still limited number of independent realizations of our simulations.

## 4. RESULTS

### 4.1. Dark Matter Bispectrum

We mainly present our results with the reduced bispectrum  $Q(k, u, \alpha)$ . Before we investigate in detail the scale and shape dependence of  $Q$ , we check the consistency between PT2 and the simulations for the equilateral triangle configurations, which are defined that  $k_1, k_2, k_3$  are in the same  $k$ -space bins. We show the scale dependence of  $Q_{\text{eq}}$  in Figure 2 where the points in different panels represent the different realizations of each simulation set from  $L1800$  to  $L600$ . The solid lines with the error bars are the mean values with variances. Here, the variances of the mean are obtained from the Gaussian uncertainties instead of the variances from different realizations in order to obtain an accurate error estimation on large scales. Although they would be underestimated on smaller scales, it does not affect our discussion because we mainly focus on the large-scale behaviors. The PT2 predictions are shown as the dashed lines, with  $Q_{\text{eq}} = 1/4 + 3\mu/4 = 0.585$  for our cosmological parameters.

From Figure 2, we note that different  $L_{\text{box}}$  simulations are consistent with each other on nonlinear scales of  $k > 0.2 h\text{Mpc}^{-1}$  where  $Q_{\text{eq}}$  deviates rapidly from the PT2 prediction as expected. But the situation is more complicated on large scales where large fluctuations from realization to realization are displayed, which is also implied by the Gaussian uncertainties shown in the figure. For the case of  $L1800$ , which clearly shows the trend

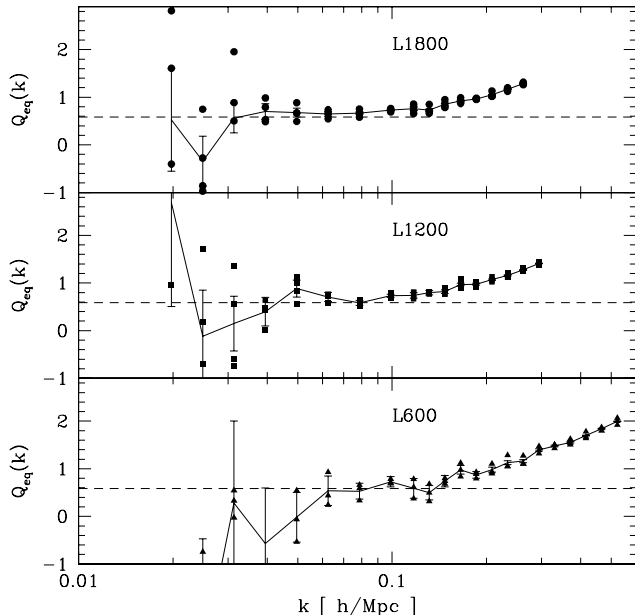


FIG. 2.— The scale dependence of  $Q_{eq}$ . The points in different panels represent the different realizations of each simulation set from  $L1800$  to  $L600$ . The solid lines with the error bars are the mean values with variances. The variances here are obtained from the Gaussian uncertainties (Equation 7). Also PT2 predictions are shown as the dashed lines.

of being constant at  $k < 0.1 \text{ hMpc}^{-1}$ , the mean of  $Q_{eq}$  is, however, still about 20% larger than that predicted by PT2 at  $0.04 \text{ hMpc}^{-1} < k < 0.1 \text{ hMpc}^{-1}$ . We also find such deviations in  $L1200$  at scales of  $0.05 \text{ hMpc}^{-1} < k < 0.1 \text{ hMpc}^{-1}$ . For  $L600$  the tendency toward constant starts from  $k \sim 0.06 \text{ hMpc}^{-1}$ , but the large fluctuation prevents us from telling whether the simulation has a similar deviation from the PT2. The jump in the errors in  $L600$  at  $0.1 \text{ hMpc}^{-1}$  is caused by our change of Fourier space bin scheme at this scale.

The fluctuation of  $Q$  among the different simulation realizations on large scales is probably due to the finite-volume effect or the scarcity of realizations for each  $L_{box}$ . From the fluctuation, we can determine the scales where enough independent triangle configurations can be constructed to get an accurate value of  $Q$ . As  $L_{box}$  changes from  $L1800$  to  $L600$ , the scales where  $Q$  can be determined are  $k > 0.03 \text{ hMpc}^{-1}$ ,  $k > 0.04 \text{ hMpc}^{-1}$ , and  $k > 0.08 \text{ hMpc}^{-1}$ , respectively if we require the errors are less than about 30%. Thus the finite-volume effect is still very important at large scales of  $k < 0.1 \text{ hMpc}^{-1}$  even for simulations with a size as large as that of  $L600$ . It would be extremely cautious to calculate the dark matter bispectrum on scales of  $k < 0.1 \text{ hMpc}^{-1}$  when using simulations with a size much smaller than that of  $L600$ . Moreover, to make an accurate measurement on scales up to  $k \sim 0.01 \text{ hMpc}^{-1}$ , we still need to involve more realizations or simulations of an even larger box size.

In Figure 3, we show the scale and shape dependence of  $Q(k, u, \alpha)$  from large to small scales with  $u \equiv k_2/k_1 = 2$ . Different points denote different  $L_{box}$  results, with circles for  $L1800$ , squares for  $L1200$ , and triangles for  $L600$ . The error bars are the variances of the mean from

the different realizations. The dashed lines represent the PT2 predictions. As we see from the figure, different  $L_{box}$  simulations are consistent with each other over all the scales. So, different simulation resolutions do not affect the measurement of  $Q$  over all the scales here. The PT2 predictions only agree well with the simulations on scales of  $k < 0.05 \text{ hMpc}^{-1}$  (where the measurement errors are also large). Starting from  $k \sim 0.06 \text{ hMpc}^{-1}$ , PT2 has already deviated from the simulation predictions, which indicates that the nonlinear effect may be important even on these large scales.

We check the influence of nonlinear corrections by simply replacing the linear power spectrum  $P_L(k)$  in Equation (4) and Equation (6) with the nonlinear power spectrum  $P_{NL}(k)$  derived directly from the simulations. The reason to do this is that in real observations, both the bispectrum and the power spectrum are nonlinearly evolved quantities. The results are shown as the solid lines in Figure 3. This nonlinear correction can improve somewhat the match between the simulations and the PT2 at scales between  $0.05 \text{ hMpc}^{-1}$  and  $0.1 \text{ hMpc}^{-1}$ , but does not remove the mismatch completely.

Despite the overall agreement of PT2 with the simulations on large scales for many different  $\alpha$  configurations, PT2 still overestimates the true  $Q(k, u, \alpha)$  for colinear triangle configurations, as shown clearly in the top left panel of Figure 3. This phenomenon was also discovered by many other authors (e.g., Scoccimarro et al. 1999; Smith et al. 2008). It may be explained by the fact that these large-scale structures tend to be filamentary rather than spherical in the simulations. For configurations near that of the isosceles triangles where  $k_3 = k_2 = 2k_1$  and  $\alpha/\pi = 0.58$ , there is, however, a trend that PT2 underestimates the bispectrum from  $k = 0.06 \text{ hMpc}^{-1}$  to  $0.1 \text{ hMpc}^{-1}$ . Such underestimates are not due to the shot-noise effect in the simulations. We have corrected for the shot-noise effect when obtaining  $Q$ . Because we have  $1024^3$  dark matter particles for each simulation, the shot noise is negligible for the final results. So, such an inconsistency demonstrates the defect of PT2 on these large scales. In the framework of perturbation theory, to describe the simulations better, we might have to incorporate higher-order corrections, such as the one-loop correction (Scoccimarro & Frieman 1996; Bernardeau et al. 2002). Involving such corrections may change the shape of  $Q$  even on large scales, i.e., to make  $Q$  smaller for colinear triangles and larger near isosceles triangles, consistent with our results (e.g., Bernardeau et al. 2008).

## 4.2. The Halo Model

### 4.2.1. Formalism

To better understand the nonlinear effects in the reduced bispectrum, we use the halo model method to theoretically study the properties of  $Q$  (Jing et al. 1998; Jing & Börner 1998; Ma & Fry 2000; Peacock & Smith 2000; Seljak 2000; Scoccimarro et al. 2001; Berlind & Weinberg 2002; Cooray & Sheth 2002; Takada & Jain 2003; Wang et al. 2004; Smith et al. 2008). The essence of the halo model is to construct the distribution of particles (dark matter or galaxies) by fixing the distribution of the clumps (dark matter halos) and the distribution of the particles within the clumps on the assumption that all the particles reside in the clumps. So, it is a halo-

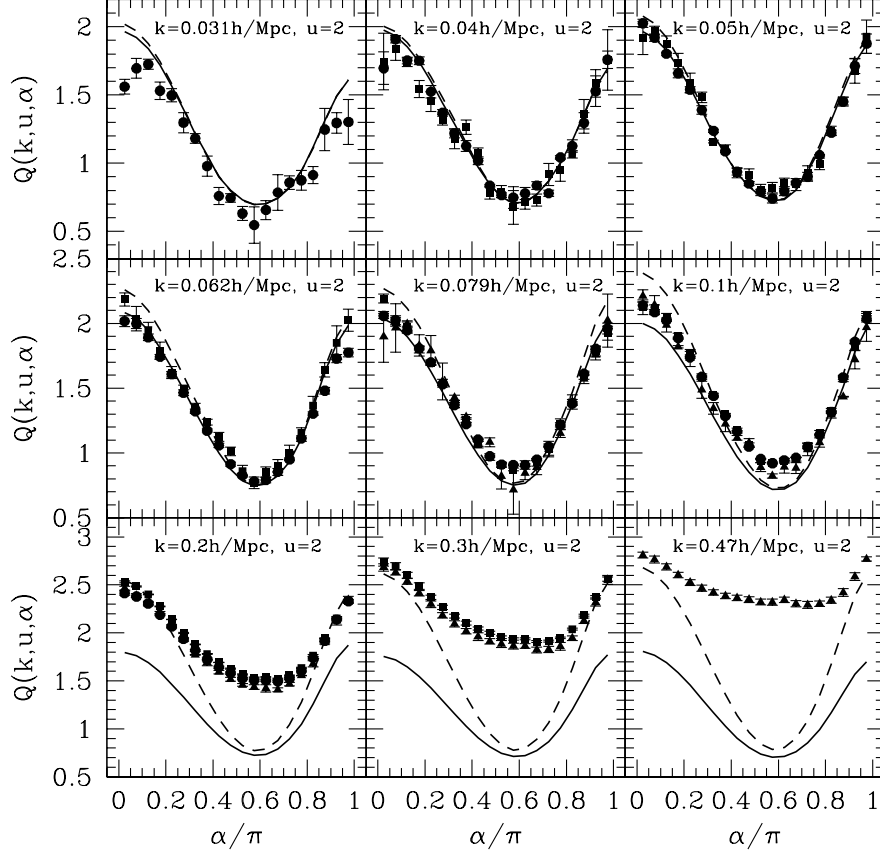


FIG. 3.— Scale and shape dependence of  $Q(k, u, \alpha)$  from large to small scales with  $u \equiv 2$ , i.e.,  $k_2 = 2k_1$ . Different points denote the results for different  $L_{box}$ , with circles for  $L1800$ , squares for  $L1200$ , and triangles for  $L600$ . The error bars are the variances on the average of the different realizations. The dashed and solid lines represent the PT2 predictions with the linear power spectrum  $P_L(k)$  and the nonlinear power spectrum  $P_{NL}(k)$ , respectively.

based method and the changes in the properties of halos will affect the final distribution of the particles.

Such a hierarchical method is very easy to apply given the information of the different model components. The dark matter halo distribution is generally constrained by the halo mass function  $n(m)$ , which describes the dark matter halo number density  $n$  as a function of halo mass  $m$ . The particle distribution within the halos is defined by the dark matter halo density profile  $\rho(r|m)$ . So, the particle-particle correlations can be obtained from the halo-halo correlations. By assuming a biased distribution of halos relative to the underlying mass, we can describe the halo-halo correlations with the halo bias parameters  $b_i(m)$  ( $i = 1, 2, \dots$ ) (Mo, Jing & White 1997; Sheth & Tormen 1999).

Following the notation described by Cooray & Sheth (2002), the dark matter power spectrum can be decomposed into the 1-halo and 2-halo terms as

$$P(k) = P_{1h}(k) + P_{2h}(k). \quad (8)$$

These terms are

$$\begin{aligned} P_{1h}(k) &= M_{02}(k, k) \\ P_{2h}(k) &= [M_{11}(k)]^2 P_L(k), \end{aligned} \quad (9)$$

where

$$\begin{aligned} M_{ij}(k_1, \dots, k_j) &\equiv \int dm n(m) \left( \frac{m}{\bar{\rho}} \right)^j b_i(m) \\ &\times [u(k_1|m) \dots u(k_j|m)]. \end{aligned} \quad (10)$$

and  $b_0 \equiv 1$ .

Here,  $\bar{\rho}$  is the mean density of the universe and  $u(k|m)$  is the normalized Fourier transform of the dark matter halo density profile  $\rho(r|m)$  truncated at the virial radius  $r_{vir}$ ,

$$u(k|m) = \int_0^{r_{vir}} dr 4\pi r^2 \frac{\sin kr}{kr} \frac{\rho(r|m)}{m}. \quad (11)$$

As  $k \rightarrow 0$ ,  $u(k|m) \rightarrow 1$  and by definition, we have

$$M_{11}(k) \rightarrow \int dm n(m) \frac{m}{\bar{\rho}} b_1(m) = 1, \quad (12)$$

and so on large scales  $P_{2h}(k) \rightarrow P_L(k)$ , as expected.

The bispectrum is similarly decomposed into the contributions from the 1-halo, 2-halo, and 3-halo terms,

$$B_{123} = B_{1h} + B_{2h} + B_{3h}, \quad (13)$$

where

$$\begin{aligned}
B_{1h} &= M_{03}(k_1, k_2, k_3), \\
B_{2h} &= M_{11}(k_1)M_{12}(k_2, k_3)P_L(k_1) + \text{cyc.}, \\
B_{3h} &= M_{11}(k_1)M_{11}(k_2)M_{11}(k_3)B_{PT} \\
&\quad + [M_{11}(k_1)M_{11}(k_2)M_{21}(k_3)P_L(k_1)P_L(k_2) + \text{cyc.}].
\end{aligned} \tag{14}$$

Again we have  $B_{3h} \rightarrow B_{PT}$  as  $k \rightarrow 0$ , which means that the 3-halo term will return to that of the PT2 predictions on large scales.

The reduced bispectrum  $Q$  is then defined as

$$Q(k_1, k_2, k_3) = \frac{B_{123}}{P(k_1)P(k_2) + \text{cyc.}}. \tag{15}$$

Note the difference from Equation (6) in the denominator where the linear power spectrum  $P_L(k)$  is replaced by the nonlinear power  $P(k)$  determined in the halo model.

In our model, dark matter halos are defined as objects with a mean density  $\Delta_{vir}$  times that of the background universe (Bryan & Norman 1998), where  $\Delta_{vir} \approx 361$  for our cosmology parameters, and their density distribution follow the Navarro–Frenk–White (NFW) profile (Navarro, Frenk, & White 1996). The concentration parameter  $c(m)$  in the density profile is given by the relation  $c(m) = c_0(m/m_*)^\beta$ , where  $c_0 = 9$ ,  $\beta = -0.13$ , and  $m_* = 4.8 \times 10^{12} h^{-1} \text{M}_\odot$  is the nonlinear mass scale (Bullock et al. 2001). We also generate the linear power spectrum from CMBfast here.

For the halo mass function (MF), first we consider the two commonly used analytical models of Press & Schechter (1974) (PS) and Sheth & Tormen (1999) (ST). They are defined by

$$n(m)dm = \frac{\bar{\rho}}{m} f(\nu) d\nu, \tag{16}$$

where  $\nu = \delta_c/\sigma(m)$ , with  $\delta_c = 1.69$ , the spherical collapse threshold of the linear overdensity  $\delta$ .  $\sigma(m)$  is the linear rms fluctuation within spheres of radius  $R = (3m/4\pi\bar{\rho})^{1/3}$ ,

$$\sigma^2(m) = \int \frac{dk}{k} \frac{k^3 P_L(k)}{2\pi^2} W^2(kR), \tag{17}$$

where  $W(x) = 3(\sin x - x \cos x)/x^3$  is the Fourier transform of the top-hat window function and  $W(x) \rightarrow 1$  as  $x \rightarrow 0$ .

The function  $f(\nu)$  for PS and ST can be generalized into the following form:

$$\nu f(\nu) = 2A \sqrt{\frac{a\nu^2}{2\pi}} [1 + (a\nu^2)^{-p}] \exp\left(-\frac{a\nu^2}{2}\right) \tag{18}$$

where  $A = 1, 0.322$ ,  $p = 0, 0.3$ , and  $a = 1, 0.707$  for PS and ST, respectively.

Jenkins et al. (2001) have also derived the halo mass functions for different halo definitions of FOF halos and spherical overdensity (SO) halos. Here, we only use their FOF halo mass function to match our halo definition

$$\nu f(\nu) = 0.307 \exp(-|\ln(\nu/\delta_c) + 0.61|^{3.82}), \tag{19}$$

with  $-0.9 \leq \ln(\nu/\delta_c) \leq 1.0$ , corresponding to about  $4 \times 10^{11} h^{-1} \text{M}_\odot \leq m \leq 4 \times 10^{15} h^{-1} \text{M}_\odot$  in our simulations. Although this mass function is derived within a finite halo mass range and does not satisfy the density normalization requirement, we can still impose the normalization constraint of Equation (12) by only integrating over a limited mass range, i.e.,

$$\begin{aligned}
\int_0^\infty dm n(m) \frac{m}{\bar{\rho}} b_1(m) &= \int_{M_1}^{M_2} dm n(m) \frac{m}{\bar{\rho}} b_1(m) + \\
&\quad \left[ 1 - \int_{M_1}^{M_2} dm n(m) \frac{m}{\bar{\rho}} b_1(m) \right].
\end{aligned} \tag{20}$$

The upper mass limit  $M_2$  is usually set by the maximum halo mass in the simulations. Here, we just use the maximum halo mass seen in *L1800* as  $M_2 = 6 \times 10^{15} h^{-1} \text{M}_\odot$ .

For the halo bias parameters, we use the results of Mo, Jing & White (1997) and Sheth & Tormen (1999). We only need to consider the first two halo bias parameters:

$$b_1(m) = 1 + \epsilon_1 + E_1, \tag{21}$$

$$b_2(m) = 2(1 + a_2)(\epsilon_1 + E_1) + \epsilon_2 + E_2, \tag{22}$$

where

$$\epsilon_1 = \frac{a\nu^2 - 1}{\delta_c}, \quad \epsilon_2 = \frac{a\nu^2}{\delta_c^2} (a\nu^2 - 3),$$

$$E_1 = \frac{2p/\delta_c}{1 + (a\nu^2)^p}, \quad \frac{E_2}{E_1} = \frac{1 + 2p}{\delta_c} + 2\epsilon_1,$$

$$\text{and} \quad a_2 = -17/21. \tag{23}$$

As for the Jenkins et al. (2001) MF (hereafter JMF), we also use the bias parameters corresponding to the PS MF. Changing to the other halo bias model does not significantly affect the predictions for the power spectrum or bispectrum.

We compare the three mass functions with our simulations for  $m^2 n(m)/\bar{\rho}$  in Figure 4, where different points stand for different  $L_{box}$  simulations and different lines for different mass functions. The error bars are determined from the scatter among the different realizations. The fluctuations shown in the low mass ends of different  $L_{box}$  simulations are caused by our lowest mass halo definitions that we set 10 particles as the minimum requirement for a bound halo. Except for the PS MF, the other MFs have similar halo number densities at the high mass end, though JMF is somewhat smaller than ST MF for  $m > 10^{15} h^{-1} \text{M}_\odot$ . The figure indicates that PS MF has much fewer large halos while retaining too many small mass halos. The ST MF is consistent with the simulations for the high mass and low mass halos, but it is substantially lower in the range of  $10^{13} h^{-1} \text{M}_\odot - 10^{15} h^{-1} \text{M}_\odot$ , which is quite important for the scales we consider here. JMF seems to agree with the simulations better for these intermediate masses, though in a detailed comparison we find that it is still lower than the simulations for  $m > 10^{13} h^{-1} \text{M}_\odot$ .

In our simulations, about 20%–30% of the total halo particles reside in halos with  $m \geq 10^{14} h^{-1} \text{M}_\odot$  and about

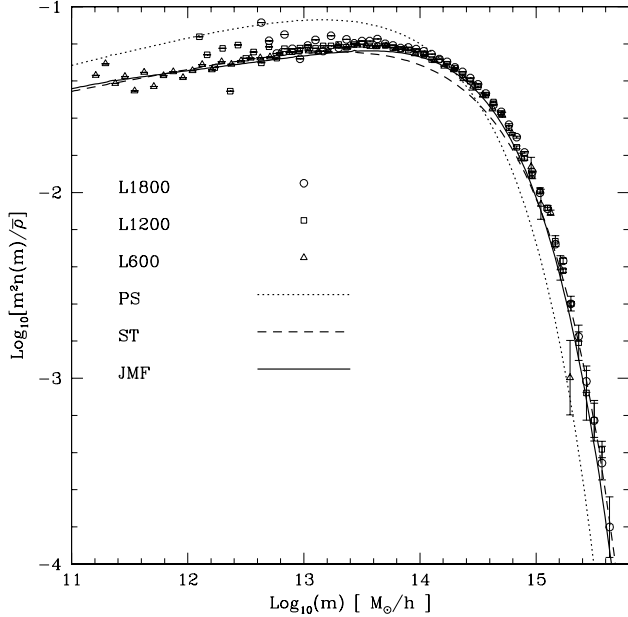


FIG. 4.— Three mass functions compared with our simulations. Different points stand for different  $L_{box}$  simulations and different lines for different mass functions

53%–80% are in halos of  $m \geq 10^{13} h^{-1} M_{\odot}$ . The fluctuations are due to the different resolutions of different  $L_{box}$  simulations. Therefore, the differences among different MFs in the mass range of  $10^{13} h^{-1} M_{\odot}$ – $10^{15} h^{-1} M_{\odot}$  will strongly affect the final results at least in the intermediate scales as shown in Figure 5. Although we do not have a mass function exactly consistent with the simulations, we can still compare the results of  $Q$  for these three MFs to study the effect of different halo mass distribution.

#### 4.2.2. The Halo Model Results

After specifying the MF and the halo bias, we can theoretically determine the power spectrum and the bispectrum of the dark matter. In Figure 5, we show the ratio between the nonlinear power spectrum  $P(k)$  and the linear power  $P_L(k)$  for halo models of different MFs, compared with those of the simulations. The wiggles on the large scales are caused by the fact that the Baryonic Acoustic Oscillations (BAO) features are suppressed in the nonlinear evolution relative to the linear evolution. The nonlinear power spectrum from the simulations is a bit smaller than the linear power on large scales (corresponding to the first BAO peak), and it rapidly increases when  $k > 0.1 h\text{Mpc}^{-1}$ . The halo models for different MFs converge on large scales where the 2-halo term dominates. But they are still larger than the linear power spectrum, because the 1-halo term still has a nonvanishing contribution to  $P(k)$  on these large scales. Compared with the simulations, the power spectra of the halo models are larger than those of the simulations, and the wiggles in  $k > 0.1 h\text{Mpc}^{-1}$  where the 1-halo term becomes important are not as evident as in the simulations. For scales of  $k > 0.2 h\text{Mpc}^{-1}$ , all the halo model predictions are substantially lower than those of the simulations. On such scales, the large mass halos play an important role in the 1-halo term. And yet we have not corrected for the

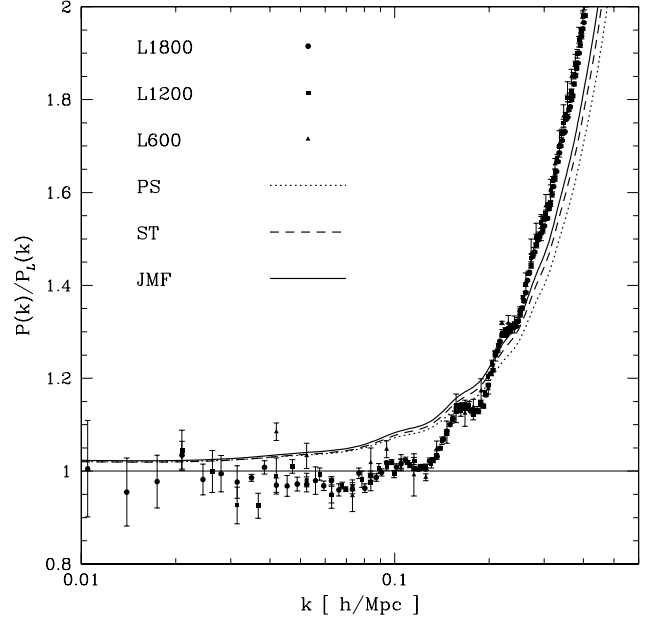


FIG. 5.— Ratio between the nonlinear power spectrum  $P(k)$  and the linear power  $P_L(k)$  for the halo model predictions with different MFs, compared with those of the simulations.

halo boundary and exclusion effects (e.g., Takada & Jain 2003) in the halo models. The effect of choosing an MF is relatively small, as the predicted power spectra based on the three MFs are very similar. The simple analytical prescription of the halo model, instead of its ingredients (the MF, the halo density profile, and the halo bias factors), may be the main cause leading to the discrepancies between the models and the simulations shown in Figure 5.

In Figure 6, we show the halo model predictions for the reduced bispectrum  $Q(k, u, \alpha)$ . As in Figure 3, the points are for the simulations. The dotted, dashed, and solid lines show the halo model predictions for PS, ST, JMFs respectively. Compared with the PT2 predictions in Figure 3, the halo models are a bit larger on large scales, as shown in the top panels of Figure 6. Different halo model predictions converge on the large scales where the 3-halo term dominates. But the predictions of the JMF model are somewhat larger than the others. It is generated by the fact that the 2-halo term contribution is much higher for JMF. Such differences are shown clearly in the intermediate scales of  $0.06$ – $0.1 h\text{Mpc}^{-1}$  in the middle panels of Figure 6. On these scales, the halo models capture the shape of reduced bispectrum in the simulations rather well compared with the PT2 predictions, though the amplitudes are still higher than expected. The result for the PS MF seems to fit with the simulation bispectrum better near the isosceles triangle shapes. For the quasi-linear and nonlinear scales of  $0.2$ – $0.5 h\text{Mpc}^{-1}$  in the bottom panels of Figure 6, the differences between the MFs show up distinctly. The model predictions for the PS MF are in much better agreement with the simulations. Even at the highly nonlinear scale of  $k \sim 0.5 h\text{Mpc}^{-1}$ , it can provide a fairly good estimate of  $Q$ . And as  $k$  increases, the reduced bispectra of the simulations approach a constant more slowly

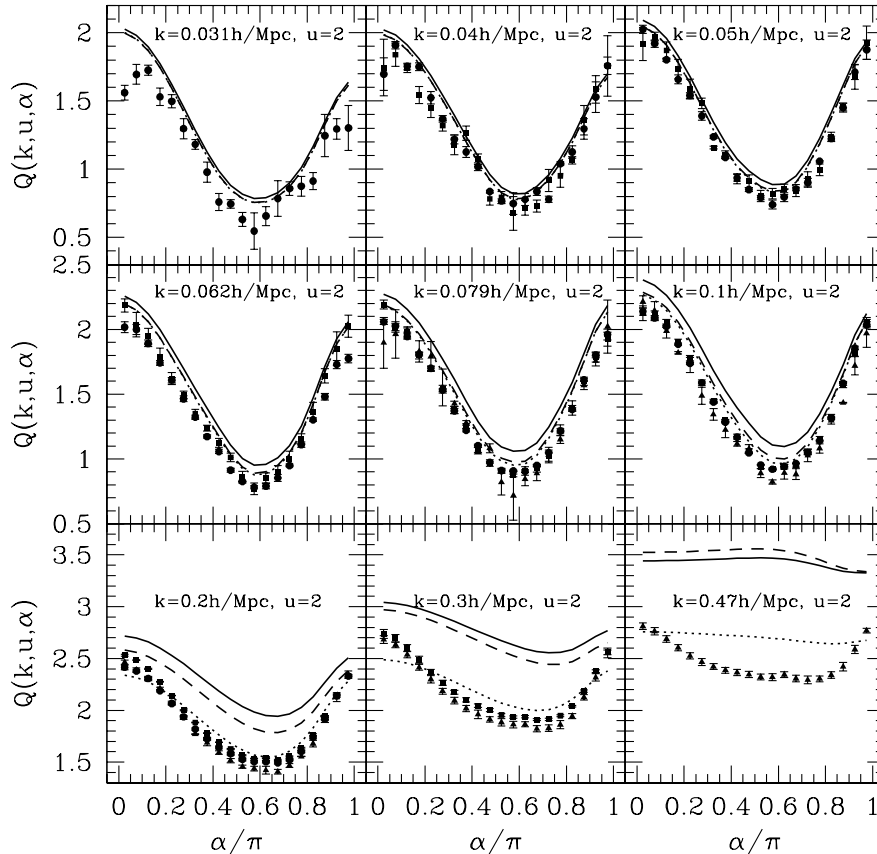


FIG. 6.— Same as Figure 3, but for the halo model predictions with different MFs. The points are for the simulation results. The dotted, dashed, and solid lines show the halo model predictions with PS, ST, JMFs respectively.

than the halo models predict. Moreover, the turnover feature in the shape dependence, appeared in the halo model predictions for the ST and JMFs at the scale of  $k \sim 0.5 h\text{Mpc}^{-1}$ , is not seen in the simulations.

The better agreement on the reduced bispectrum between the halo model predictions for the PS MF and the simulations on scales of  $k > 0.2 h\text{Mpc}^{-1}$  does not mean that PS MF is a better description for the mass function in halo models. Since the reduced bispectrum is the ratio of bispectrum to a sum of power spectrum products, the better agreement achieved with the PS MF is largely a coincidence, because the power spectra are fitted worse on relevant scales by the PS model (as shown in our Figure 5). In fact, the ST MF and JMF better describe the mass function of halos in our simulations (Figure 4). We also note that our result is consistent with Fosalba et al. (2005), who argued that a better agreement in the reduced bispectrum between the halo model and simulations can be achieved by imposing a mass cutoff for halos at the high mass end. But, we do not think that imposing the mass cutoff is physical in our study, since our simulation box is big enough that the halos at high mass end of ST MF (or JMF) are fairly well sampled in our simulations. Therefore, the failure of the halo model for the ST MF or JMF implies the inherent difficulty of the halo models to accurately predict the power spectrum and the bispectrum.

To investigate the effects of choosing different MFs

and the contributions of different halo terms, we show in Figure 7 the scale and shape dependence of  $B_{ih}/B_{123}$  of each halo term by changing  $k$  and  $\alpha$  while fixing  $\mu \equiv k_2/k_1 = 2$ . We show from top to bottom for three triangle shapes including the colinear and isosceles triangles, specified by different  $\alpha$  values. At the scale  $k = 0.01 h\text{Mpc}^{-1}$ , in each panel from top to bottom are the 3-halo, 2-halo, and 1-halo term contributions. Different lines denote the halo model predictions for different MFs as in Figures 5 and 6. On large scales of  $k < 0.1 h\text{Mpc}^{-1}$ , the 3-halo term dominates but 2-halo term still has a contribution of about 5%–20% in these halo models. Comparing Figure 3 and Figure 6, it seems that the 2-halo term contributions in the halo models are higher than simulations predict. Furthermore, we note that in the determination of the reduced bispectrum  $Q(k, u, \alpha)$  of the halo models, the linear power spectrum  $P_L(k)$  in the denominator of Equation (6) in PT2 is replaced by the nonlinear power  $P(k)$  which is larger than  $P_L(k)$  over all the scales shown in Figure 5. Therefore, the 2-halo term is actually necessary to fit with the simulations, otherwise only using the 3-halo term ( $B_{3h} \rightarrow B_{PT}$  on large scales) will make  $Q(k, u, \alpha)$  of the halo models much smaller than those of simulations. For the different halo term contributions, the differences among choosing different MFs are very small on large scales. The PS and ST MFs have nearly the same halo-term contributions at these scales. This indicates that



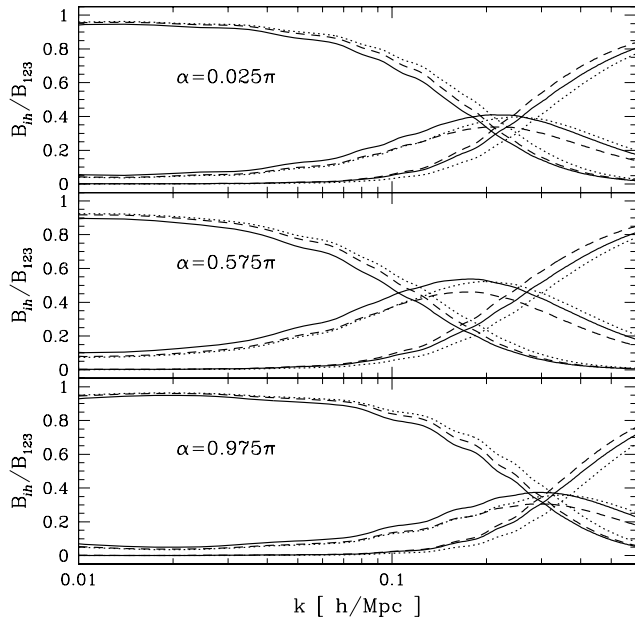


FIG. 7.— Scale and shape dependence of each halo term contribution  $B_{ih}/B_{123}$  with  $\mu \equiv k_2/k_1 = 2$ , as well as the effects of the different MFs. We show from top to bottom for three triangle shapes including the colinear and isosceles triangles, specified by different  $\alpha$  values. At scale  $k = 0.01 h\text{Mpc}^{-1}$ , in each panel from top to bottom are the 3-halo, 2-halo, and 1-halo term contributions. Different lines denote the results for different MFs as in Figure 5 and Figure 6.

the bispectrum on these scales is not sensitive to the choice of MFs.

When  $k > 0.1 h\text{Mpc}^{-1}$ , we see from Figure 7 that the 2-halo term is much more important for the isosceles triangle shapes than for the colinear ones. It has almost the same contribution as the 3-halo term at  $k \sim 0.1 h\text{Mpc}^{-1}$  for isosceles shapes, while the 3-halo term still dominates in the colinear configurations. Thus, it explains the failure of PT2 which only includes the 3-halo term for the isosceles triangles, shown in the middle panels of Figure 3. On these quasi-linear scales, the 1-halo term also starts to become important and its contribution differs for different triangle shapes, which clearly shows the influence on the shape dependence of  $Q(k, u, \alpha)$ . Again, the 1-halo term is most important for the isosceles triangle configurations. We can therefore infer that the nonlinear effect is more significant for such triangle shapes. Meanwhile, the differences also emerge on these quasi-linear scales when different MFs are used. We note from Figure 6 that the reduced bispectrum for the ST MF case increases rapidly in the quasi-linear and nonlinear regime. From Figure 7, we can see that it is caused by the rapid increase in the 1-halo term contribution. Even in the nonlinear scale of  $k = 0.5 h\text{Mpc}^{-1}$ , where the 1-halo term is dominant, the 2-halo contribution is still not negligible and the 3-halo term also has a nonvanishing contribution for some triangle configurations.

Despite the fact that the halo model can provide a qualitative explanation for  $Q(k, u, \alpha)$  down to the quasi-linear scales, there still exist unavoidable problems with the halo model if we consider the possibility that the halo model can match the power spectrum  $P(k)$  of the

simulations extremely well. We take  $k = 0.1 h\text{Mpc}^{-1}$  for example. We see from Figure 5 that the nonlinear power  $P(k)$  of the simulations is almost equal to the linear power  $P_L(k)$ , only with a small deviation at this scale. Then we can replace  $P(k)$  in Equation (15) with  $P_L(k)$ . Thus, the reduced bispectrum  $Q(k, u, \alpha)$  must be larger than  $Q_{PT}$  in PT2, because the 3-halo term has already included  $B_{PT}$  (at this scale  $M_{11}(k)$  is still very close to 1) but the 2-halo term can even add an additional sizable contribution. For the case of colinear configurations with  $\alpha \rightarrow 0$ , in Figure 3, the PT2 prediction is much larger than those of the simulations. Therefore, the halo model prediction with the 2-halo term included would give an even larger bispectrum. This apparent contradiction in the predictions for  $P(k)$  and  $Q(k, u, \alpha)$  between the halo models and the simulations actually comes from the prescription of the halo model. Because in the halo model, it includes the PT2 predictions in the 3-halo term in Equation (14). The failure of PT2 will then lead to the failure of the halo model if its predictions are larger than the simulations. Moreover, the 2-halo term and even the 1-halo term are not negligible at relevant large scales.

## 5. DISCUSSIONS AND CONCLUSIONS

We use a set of numerical  $N$ -body simulations to study the large-scale behavior of the reduced bispectrum  $Q(k, u, \alpha)$  and compare it with the analytical predictions from both the second-order perturbation theory (PT2) and the halo models. We investigate the scale and shape dependence of  $Q$  and find that although PT2 agrees fairly well with the simulations on the large scales of  $k < 0.05 h\text{Mpc}^{-1}$ , it still shows a signature of deviation as the scale goes down. Even on the largest scale where the bispectrum can be explored with our simulations, the inconsistency between PT2 and the simulations appears for the colinear triangle shapes. The better agreement of PT2 with the simulations after the nonlinear power spectrum is used for the PT2 implies the importance of nonlinear effects even on these large scales of  $k < 0.1 h\text{Mpc}^{-1}$ , which is a supplement to the previous studies (e.g., Bernardeau et al. 2002; Smith et al. 2008). Then one of our main conclusions is that higher-order corrections (e.g., loop corrections) are necessary on large scales of  $k = 0.05\text{--}0.1 h\text{Mpc}^{-1}$  for the perturbation theories to predict  $Q$  at an accuracy of percent level.

An alternative method of predicting the reduced bispectrum is through the halo model with several basic ingredients. After a detailed comparison between the predictions and our simulation results, however, we are disappointed to find that halo models can at best serve as a qualitative method to help study the behavior of  $Q$  on large scales and also on relatively small scales. But because of the nonnegligible two-halo term contribution, the halo model predictions of the reduced bispectrum are always higher than the results of the simulations. No halo model can be brought into agreement with the bispectrum on nonlinear scales unless a reasonable mass function is adopted.

We have carefully and accurately measured the bispectrum for a large range of scales in the simulations. The results could be useful for future analytical modeling of  $Q$ . Therefore, a table of  $Q$  from our measurement is made available at

<http://www.shao.ac.cn/mppg/guo/paper/dmbisp.html>.

We thank Jun Pan and Roman Scoccimarro for useful discussions. This work is supported by NSFC (10533030,

10821302, 10873028, 10878001), by the Knowledge Innovation Program of CAS (no. KJCX2-YW-T05), and by 973 Program (no.2007CB815402).

#### REFERENCES

- Berlind, A. A. & Weinberg, D. H. 2002, *ApJ*, 575, 587  
 Bernardeu, F., Colombi, S., Gaztañaga, E., & Scoccimarro, R., 2002, *Phys. Rep.*, 367, 1  
 Bernardeu, F., Crocce, M., & Scoccimarro, R. 2008, *Phys. Rev. D*, 78, 103521  
 Bryan, G., Norman, M. 1998, *ApJ*, 495, 80  
 Bullock, J. S., Kolatt, T. S., Sigad, Y., Somerville, R. S., Klypin, A. A., Primack, J. R., Dekel, A. 2001, *MNRAS*, 321, 559  
 Cooray, A., Sheth, R. 2002, *Phys. Rep.*, 372, 1  
 Fosalba, P., Pan, J., Szapudi, I. 2005, *ApJ*, 632, 29  
 Fry, J. N. 1984, *ApJ*, 279, 499  
 Fry, J. N., Melott, A. L., Shandarin, S. F. 1993, *ApJ*, 412, 504  
 Hou, Y. H., Jing, Y. P., Zhao, D. H., & Börner 2005, *ApJ*, 619, 667  
 Jenkins, A., Frenk, C. S., White, S. D. M., Colberg, J. M., Cole, S., Evrard, A. E., Couchman, H. M. P., & Yoshida, N. 2001, *MNRAS*, 321, 372  
 Jing, Y. P. & Börner, G. 1998, *ApJ*, 503, 37  
 Jing, Y. P., & Suto, Y. 1998, *ApJ*, 494, L5  
 Jing, Y. P., Mo, H. J., & Boerner, G. 1998, *ApJ*, 494, 1  
 Jing, Y. P., & Suto, Y. 2000, *ApJ*, 529, L69  
 Jing, Y. P., & Suto, Y. 2002, *ApJ*, 574, 538  
 Jing, Y. P., Suto, Y., & Mo, H. J. 2007, *ApJ*, 657, 664  
 Ma, C., & Fry, J. N. 2000, *ApJ*, 543, 503  
 Mo, H. J., Jing, Y. P., White, S. D. M., 1997, *MNRAS*, 290, 651  
 Navarro, J. F., Frenk, C. S., & White, S. D. M. 1996, *ApJ*, 462, 563  
 Nichol, R. C., et al. 2006, *MNRAS*, 368, 1507  
 Peacock, J. A., & Smith, R. E. 2000, *MNRAS*, 318, 1144  
 Peebles, P. J. E. 1980, *The Large-Scale Structure of the Universe*(Princeton: Princeton Univ. Press)  
 Press, W. H., & Schechter, P. 1974, *ApJ*, 187, 425  
 Scoccimarro, R., & Frieman, J. 1996, *ApJ*, 105, 37  
 Scoccimarro, R., Colombi, S., Fry, J. N., Frieman, J. A., Hivon, E., Melott, A. 1998, *ApJ*, 496, 586  
 Scoccimarro, R., Couchman, H. M. P., Frieman, J. A. 1999, *ApJ*, 517, 531  
 Scoccimarro, R., Sheth, R. K., Hui, L., & Jain, B. 2001, *ApJ*, 546, 20  
 Scoccimarro, R., Sefusatti, E., Zaldarriaga, M. 2004, *Phys. Rev. D*, 69, 103513  
 Sefusatti, E., & Komatsu, E., 2007, *Phys. Rev. D*, 76, 083004  
 Sefusatti, E., & Scoccimarro, R., 2005, *Phys. Rev. D*, 71, 063001  
 Seljak, U. 2000, *MNRAS*, 318, 203  
 Seljak, U., & Zaldarriaga, M., 1996, *ApJ*, 469, 437  
 Sheth, R. K. & Tormen, G. 1999, *MNRAS*, 308, 119  
 Smith, R. E., Sheth, R. K., Scoccimarro, R. 2008, *Phys. Rev. D*, 78, 023523  
 Takada, M., Jain, B. 2003, *MNRAS*, 340, 580  
 Verde L., et al. 2002, *MNRAS*, 335, 432  
 Wang, Y., Yang, X. z., Mo, H. J., van den Bosch, F. C. & Chu, Y. 2004, *MNRAS*, 353, 287  
 Yang, X. H., Mo, H. J., & van den Bosch, F. C. 2003, *MNRAS*, 339, 1057  
 Zehavi, I., et al. 2004, *ApJ*, 608, 16  
 Zheng, Z. 2004, *ApJ*, 610, 61  
 Zheng, Z., Berlind, A. A., Weinberg, D. H., Benson, A. J., Baugh, C. M., Cole, S., Dave, R., Frenk, C. S., Katz, N. & Lacey, C. G. 2005, *ApJ*, 633, 791